JOURNAL OF PROPULSION AND POWER
Vol. 23, No. 3, May–June 2007

Jets in Crossflow Mixing Analysis Using Computational Fluid Dynamics and Mathematical Optimization

R. M. Morris,* J. A. Snyman,† and J. P. Meyer‡
University of Pretoria, Pretoria 0002, South Africa

DOI: 10.2514/1.22136

Computational fluid dynamics and mathematical optimization were used to investigate the mixing effectiveness of jets in crossflow. A numerical model was developed, validated, and calibrated against experimental measurements of a temperature distribution at different cross-sectional planes downstream of an orifice injection plane. Good agreement was obtained when the ratio between momentum and species diffusivities was varied according to the jet-to-mainstream momentum flux ratio. Numerical optimization of various double-sided jet configurations followed, using a parametric approach. The results obtained showed that changes in orifice size and spacing at a constant orifice-to-mainstream area ratio and momentum flux ratio have a significant influence on mixing effectiveness. The optimum configuration compared favorably with an empirically defined relationship between orifice spacing and momentum flux ratio. Mathematical optimization was then combined with numerical methods to predict the optimum orifice configuration. The results showed the feasibility of using a gradient-based approximation method to allow, for a given set of parameters, the systematic adjustment of design variables to achieve improvement in performance.

Nomenclature

a, A	=	area
C	=	constant
C_D	=	discharge coefficient
C_j	=	Hessian matrix
c_j	=	approximated constraint curvature of subproblem
D	=	orifice diameter
D_ϕ	=	diffusion coefficient
f	=	mixture fraction
$f(x)$	=	objective function
$g_j(x)$	=	jth inequality constraint
H	=	duct height
$h_k(x)$	=	kth equality constraint
I	=	identity matrix
J	=	jet-to-mainstream momentum flux ratio
$\dot{m}$	=	mass flow rate
N	=	number of orifices on each side
n	=	number of variables
$p(x)$	=	penalty function
R^n	=	n-dimensional real space
S	=	spacing between orifices
S_C	=	turbulent Schmidt number
T	=	temperature
V	=	velocity
X	=	downstream coordinate
$\boldsymbol{x}$	=	design vector
$x_j^{\max}$	=	maximum value of the jth design variable
$x_j^{\min}$	=	minimum value of the jth design variable
Y	=	radial coordinate
Z	=	lateral coordinate
β_k	=	penalty parameter
δ_i	=	specified move limit for ith design variable
θ	=	nondimensional temperature difference ratio
μ	=	viscosity
μ_i	=	penalty parameter
ρ	=	density
ρ_j	=	penalty parameter

Subscripts

equil	=	equilibrium
i, j, k	=	index
jet	=	jet
main	=	mainstream

Received 30 December 2005; revision received 13 December 2006; accepted for publication 22 December 2006.

*Lecturer, Department of Mechanical and Aeronautical Engineering.
†Professor, Department of Mechanical and Aeronautical Engineering.
‡Professor, Department of Mechanical and Aeronautical Engineering.

I. Introduction

JETS in crossflow have been examined extensively in the literature, both experimentally and numerically [1–5]. The application thereof ranges from exhaust plumes and effluent discharge to conventional and more modern gas turbine combustors. Over the past three decades initial studies have focused on bounded jets in crossflow as found in the mixing section or dilution zone of a conventional gas turbine combustor [6–15]. In dilution zone mixing the emphasis is on establishing a temperature profile that is not only acceptable to the turbine, but will also enhance its life span. To increase the understanding of efficient mixing, empirical correlations and analytical models were developed. The relations showed that momentum flux ratio, defined as

$$J = \frac{(\rho_{\text{jet}} V_{\text{jet}}^2)}{(\rho_{\text{main}} V_{\text{main}}^2)} \tag{1}$$

and spacing-to-duct height ratio (S/H) control the mixing rate and jet penetration. It was found that jet penetration and center plane profiles of temperature were similar when orifice spacing and the square root of the momentum flux ratio were inversely proportional [16].

$$C = (S/H)\sqrt{J} \tag{2}$$

The optimum value of the constant C, which provides the best mixing was determined for both single- and double-sided rows of jets as well as staggered and inline configurations. A value of C above or below the optimum corresponds to over- or underpenetration of the jets into the mainstream flow, respectively.

With the ever-increasing need for lower emissions being one of the driving forces in combustor design, dilution-mixing studies have

also been extended to combustor concepts such as the rich-burn/quick-mix/lean-burn (RQL) combustor [17–19]. This combustor has a primary zone that operates fuel rich at an equivalence ratio of 1.2:2. The products of combustion, which have high concentrations of carbon monoxide, flow into the quick-mix region and are mixed with the residual air. The combustion process is completed in the lean-burn zone. For the RQL combustor to operate efficiently, rapid and uniform mixing in the quick-mix region is critical. If the mixing in this region is not good, stoichiometric pockets at high temperatures can appear, generating large amounts of NO. Also, if the mixing is not uniform, hot spots may be produced which may severely degrade the combustor liner material as well as the turbine blades downstream. To optimize the RQL as well as more conventional combustors to adhere to these requirements, orifice size, shape, spacing, and the layout of the jets need to be considered. These variables are intricately linked to jet penetration and mixing and therefore most of the major combustion mechanisms. It has been shown that Eq. (2) also holds true for the RQL combustor although the constant C differs [20]. This is attributed to the higher jet-to-mainstream mass flow ratio.

A number of nonreacting rapid mixing studies have therefore focused on obtaining the optimum value of C for different slot configurations. Bain et al. [21] numerically investigated the effect of straight and slanted slots in a rectangular duct, as it is believed that slanted slots impose a swirl on the flowfield, which enhances the mixing, albeit at reduced jet penetration. In terms of overall unmixedness it was found that parallel slanted slots and straight slots are nearly equal. A numerical parametric study was also performed to address the question of which lateral arrangement produces superior mixing: inline or staggered [20]. This was done for straight slots with a fixed aspect ratio of 4:1. The study was also extended to investigate the effect of different slot aspect ratios on mixing performance [22]. Although most of the aforementioned studies focused on rectangular geometries, representative of an annular combustor, a number of mixing studies have also looked at cylindrical ducts [23,24].

Various detailed mixing studies have thus been performed, searching for an optimal orifice configuration. However, it has been found that little or no investigations have been done in the past where computational fluid dynamics (CFD) and mathematical optimization were combined. Most of the aforementioned numerical mixing studies have followed a parametric approach where the variables of interest were systematically varied, and the associated performance assessed. This approach does not always guarantee an optimal solution, and the number of variables considered concurrently is usually limited. Lately, combining CFD and mathematical optimization has received much attention, extending the use thereof to applications other than aerodynamic-shape optimization [25,26]. Combining CFD and mathematical optimization allows performance trends with respect to these variables to be taken into account automatically and could therefore prove to be a very powerful tool.

The purpose of this study is to optimize a simplified mixing region of a conventional gas turbine combustor, combining CFD and a gradient-based mathematical optimization algorithm. Although the geometry considered is simplified, the solution is nontrivial. As part of the study, the ability to numerically model jets in crossflow is investigated, upon which a parametric study is done to optimize double-sided jets in crossflow. The results from the parametric study are then used as input to the mathematical optimization.

II. Numerical Model

A. Computational Domain and Boundary Conditions

The geometry investigated is according to that used in the dilution jet-mixing program [6–9], where cold jet flow was injected into a heated crossflow using a rectangular duct with width and height of 304.8 and 101.6 mm, respectively. Interchangeable dilution orifice plates were used, which allowed different orifice configurations to be tested. Mixing effectiveness was quantified through total temperature measurements, obtained with a traversing rake, which allowed measurements in the radial, lateral, and axial directions. The selected computational domain extended from the center plane of an orifice to the midplane between adjacent orifices, that is, half of the orifice spacing (S) as shown Fig. 1. Symmetrical boundary conditions were specified on both lateral planes (Y–X plane). In the axial direction the domain extended between 18D and 29D downstream of the jet or orifice diameter D. A number of computations were performed and compared as the locations of the inlet and outlet boundaries were varied. The domain was further simplified for double-sided jets by assuming a symmetrical distribution about the midplane in the radial direction, consequently reducing the computational effort. This was based upon results which showed that buoyancy and gravitational forces have a negligible influence on the flowfield.

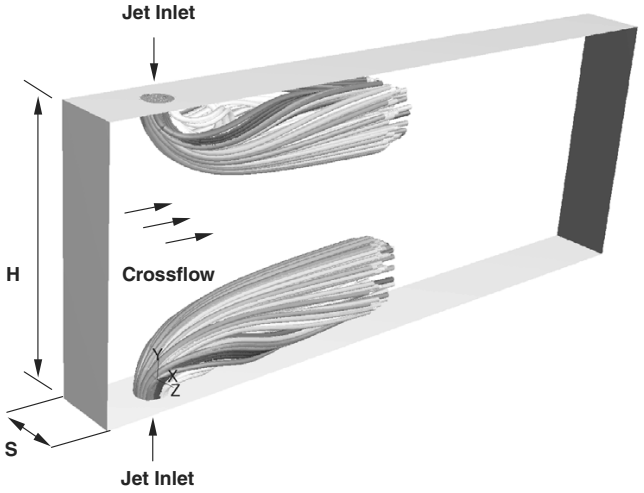

Fig. 1 Flow geometry with double-sided in-line jets.

A uniform velocity was specified at the jet and mainstream inlets along with temperature and turbulence level. A sensitivity analysis was done by varying the turbulence intensities at the jet and mainstream inlets between 1 and 10%, without any appreciable difference in the results. The top and bottom walls were assumed as adiabatic and at the outlet a zero diffusive flux normal to the exit plane was specified. Several grid sizes, ranging between 30,000 and 1.2×10^6 computational cells, were employed to verify solution independency on the mesh size. A typical mesh used during the validation process for double-sided jets contained approximately 250,000 cells. An unstructured hexahedral grid was used with grid spacing stretched close to the walls and also along the length of the duct.

B. Computational Approach

A commercial finite volume code, FLUENT [27], was used to solve the turbulent flow transport equations and appropriate physics. The fluid was modeled as an incompressible ideal gas, as changes in absolute pressure are small, and from previous studies it was concluded that the density ratio has a secondary effect on mixing efficiency [28]. All thermal properties were specified to be temperature dependent and second-order discretisztion was used. Several turbulence models were evaluated as part of the investigation, including the standard k–ε model, renormalization-group (RNG) k–ε model, realizable k–ε model, and shear-stress transport (SST) k–ω model. It was found that the SST k–ω model provided the best turbulence closure to the Reynolds-averaged Navier–Stokes (RANS) equations and all results are therefore presented with this model. Although promising studies have been performed using large-eddy simulation (LES) it is not yet employed in routine design simulations and has therefore not been used in this study due to the increase in computational time and requirements [29].

The default criterion for convergence is a three-order magnitude drop in scaled residuals for the flow equations and 6 orders of magnitude for the energy equation. However, by monitoring the area-weighted average temperature at different planes in the axial direction of the geometry it was found that the default criterion was not sufficient and was lowered to 1×10^{-7} for energy and 1×10^{-5} for all other equations to ensure complete convergence.

Table 1 Test configurations and flow conditions [7]

Test no.	D, mm	S/D	H/D	V_{main}, m/s	T_{main}, K	V_{jet}, m/s	T_{jet}, K	C_D	J
1	12.7	2	8	15.5	645.9	28.1	310.4	0.665	6.81
2	12.7	2	8	15.6	646.6	53.3	306.8	0.65	24.94
3	12.7	2	8	15.5	646.2	104.3	303.9	0.64	101.8

C. Validation

An important parameter in mixing and combustion studies is the turbulent Prandtl or Schmidt number, which expresses the ratio between momentum and species diffusivities

$$Sc = \frac{\mu}{\rho D_\phi} \tag{3}$$

From the literature is has been found that a variety of turbulent Schmidt numbers, ranging from 0.2 to 0.9, have been used to account for scalar diffusion rates [29,30]. In most cases a recommended value between 0.8 and 0.9 is used, although He et al. [29] recommended a lower turbulent Schmidt number of 0.2, based on an investigation for a single jet in crossflow using the standard k–ε model. In this study the influence of the turbulent Schmidt number was extended to opposed rows of in-line jets.

Several test cases from the dilution jet-mixing program [7] were selected to validate and calibrate the numerical model. The test cases were performed for single- and double-sided jet arrangements with different jet-to-mainstream momentum flux ratios. Results are presented only for double-sided jet arrangements in this paper and flow conditions for three arbitrary cases are summarized in Table 1. Figures 2–4, for jet-to-mainstream momentum flux ratios J of 6.81, 24.94, and 101.8 (corresponding to J values in Table 1), demonstrate the capability of the numerical model to predict nondimensionalized jet center plane temperatures at various downstream positions. The measured and predicted temperature distributions were nondimensionalized by

$$\theta = \frac{T_{\text{main}} - T}{T_{\text{main}} - T_{\text{jet}}} \tag{4}$$

In Fig. 2 the results for a low value of $J = 6.81$ show that the jets do not initially penetrate far enough into the radial direction to mix with the crossflow in the center of the duct. This can be seen at all values of X/H as the jets start to spread in the lateral direction with downstream distance. The numerical results show that a turbulent Schmidt number of 0.85 overpredicts peak values of θ, which

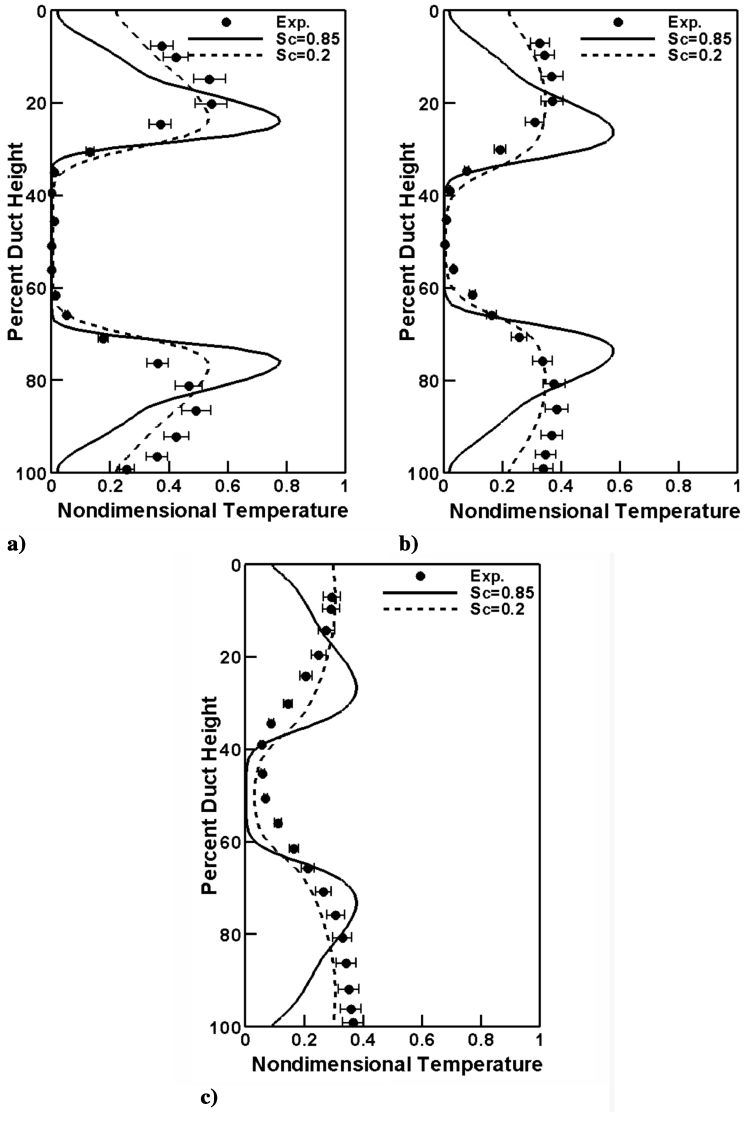

Fig. 2 Nondimensional temperature distribution for $J = 6.81$: a) $X/H = 0.25$; b) $X/H = 0.5$; c) $X/H = 1.0$.

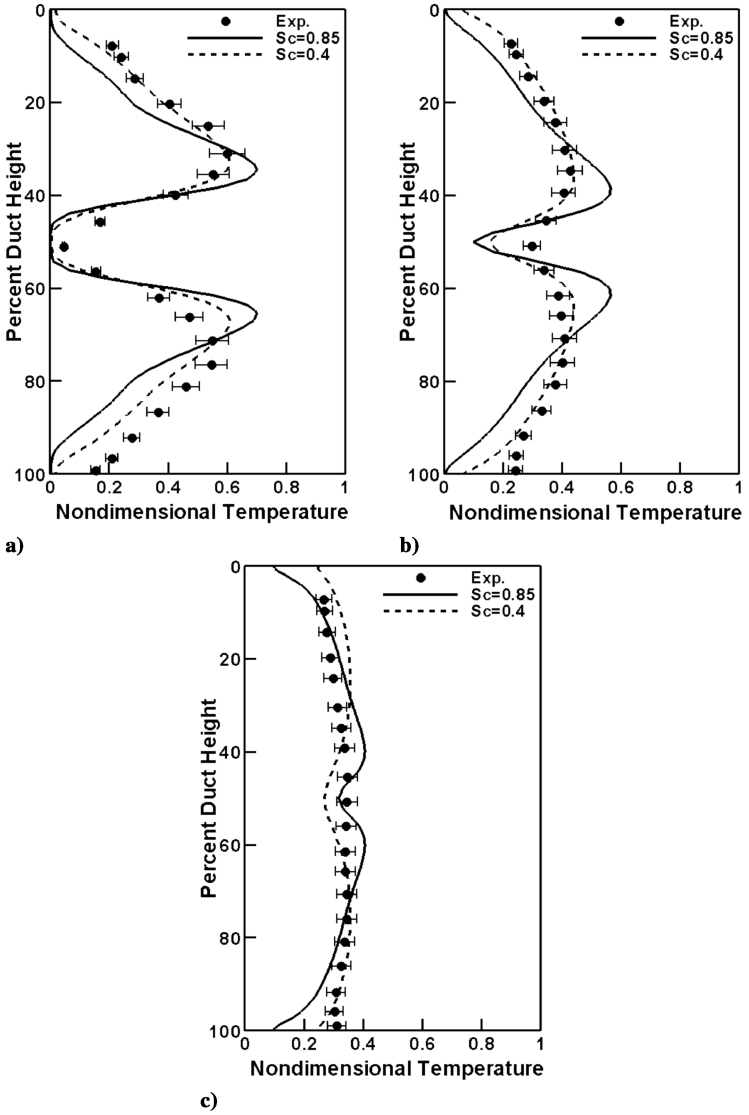

Fig. 3 Nondimensional temperature distribution for $J = 24.94$: a) $X/H = 0.25$; b) $X/H = 0.5$; c) $X/H = 1.0$.

correspond to underprediction of the lowest temperatures. Four turbulent Schmidt numbers 0.2, 0.4, 0.6, and 0.85 were tested to determine its influence on scalar mixing. It was found that by reducing the turbulent Schmidt number, the overpredicted peak values of θ were reduced and scalar mixing enhanced. The error bars depict a value within 10% of the measured results and best agreement was obtained with a value of $Sc = 0.2$ as shown. The most notable differences are observed close to the orifice injection plane, that is, $X/H = 0.25$ and near the peak values where the jets penetrate farthest into the mainstream flow. Given the turbulent nature of the jet flow these differences could be attributed to the limitations of applying a RANS approach. However, the use of plug–flow velocity profiles at the jet inlets along with effective orifice areas also contribute to a difference in predicted jet momentum. Overall, the RANS model is capable of predicting the correct trend with closer agreement obtained between measured and predicted results as the momentum flux ratio increases.

Figure 3 displays the predicted temperatures when $J = 24.94$. With J at this value, the jets penetrate farther into the radial direction to approximately 30% of the duct height (Fig. 3a) and the two streams mix fairly rapidly with downstream distance, as can be deduced from Figs. 3b and 3c. The recommended turbulent Schmidt numbers of 0.8 to 0.9 again overpredicts peak values of θ however, to a lesser extent. The best agreement was obtained with $Sc = 0.4$. It should be noted that this configuration of orifice spacing to duct height would provide the optimum mixing according to Eq. (2) where $C = 1.25$ for opposed rows of in-line jets.

Figure 4 displays the results obtained for the highest value of J, where the opposed rows of jets impinge on each other. The typical recommended value of $Sc = 0.85$ shows good agreement with the experimental measurements as well as when $Sc = 0.6$. From the validation cases it can be concluded that although a constant value of Sc of 0.8 to 0.9 is usually assumed, it is both a function of jet-to-mainstream momentum flux ratio as well as downstream distance. This is similar to the findings obtained for a single jet in crossflow [29]. At low values of J, the mixing rate is sensitive to changes in turbulent Schmidt numbers. As J increases along with downstream distance, the influence of the turbulent Schmidt number becomes less. Similar results were also obtained for single-sided injection.

III. Parametric and Mathematical Optimization

A. Parametric Optimization

A parametric CFD study was performed to analyze the mixing of opposed rows of jets in crossflow at a low jet-to-mainstream momentum flux ratio. Higher jet-to-mainstream momentum flux ratios are currently being addressed in another study and will therefore not be discussed in this paper. Results obtained were compared with the relationship defined in Eq. (2) and used as a baseline case to combine mathematical optimization with CFD mixing studies. Table 2 presents the different flow configurations along with input parameters. The geometries in Table 2 were chosen based on all configurations that would provide an equal spacing and

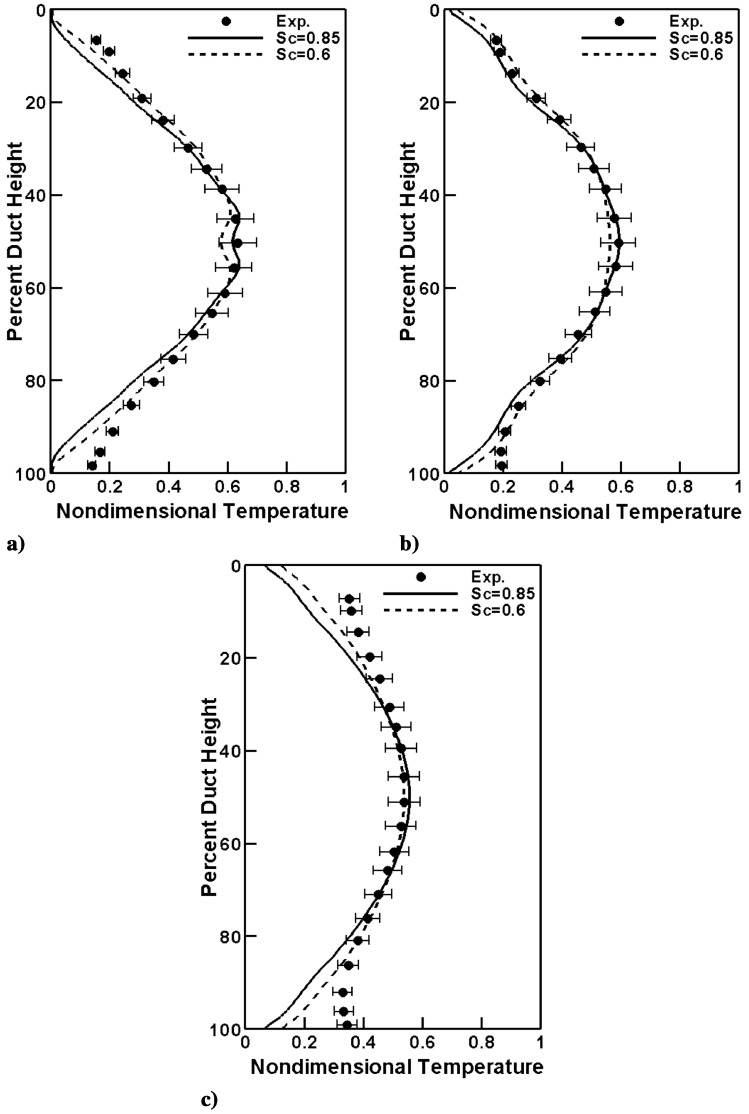

Fig. 4 Nondimensional temperature distribution for $J = 101.8$: a) $X/H = 0.25$; b) $X/H = 0.5$; c) $X/H = 1.0$.

an integer number of orifices. The number of orifices varied between 3 and 12, while keeping the total orifice area constant and $J = 10$. The importance of using an appropriate turbulent Schmidt number was previously highlighted, and the simulations were performed with $Sc = 0.2$ to account for scalar mixing at low momentum flux ratios. For comparative purposes, the simulations were also carried out for $Sc = 0.85$. Mixing effectiveness or unmixedness was quantified by an area-weighted standard deviation parameter [14] at different cross-sectional planes in the axial direction

$$\text{Mixture Uniformity} = \sqrt{\frac{1}{A}\sum_{i=1}^{n} a_i (f_i - f_{\text{equil}})^2} \tag{5}$$

Table 2 Parametric test configurations and flow conditions

N	D, mm	S/H	V_{main}, m/s	T_{main}, K	V_{jet}, m/s	T_{jet}, K	J
3	25.4	1	15	649	32.67	308	10
4	22	0.735	↓	↓	↓	↓	↓
5	19.67	0.596					
6	17.96	0.496					
7	16.63	0.429					
8	15.55	0.377					
9	14.66	0.335					
10	13.91	0.3					
11	13.26	0.271					
12	12.7	0.25	15	649	32.67	308	10

where f at each node i is the mixture fraction, defined as $1 - \theta$. The equilibrium mixture fraction is defined in terms of the equilibrium temperature, that is, the ideal temperature that would be reached when the jet and mainstream flow are perfectly mixed,

$$f_{\text{equil}} = \frac{T_{\text{equil}} - T_{\text{jet}}}{T_{\text{main}} - T_{\text{jet}}} \tag{6}$$

and

$$T_{\text{equil}} = \frac{\dot{m}_{\text{jet}} T_{\text{jet}} + \dot{m}_{\text{main}} T_{\text{main}}}{\dot{m}_{\text{jet}} + \dot{m}_{\text{main}}} \tag{7}$$

Absolute mixing is therefore approached as the mixture uniformity approaches zero across a plane. It is important to note that the definition of f_{equil} is only valid downstream of the orifices' trailing edge when all the jet flow has been added. Mixture uniformity results are therefore presented downstream of the orifices beginning at an axial plane of $X/H = 0.25$. Other mixing parameters such as pattern factor [31] and the mixing efficiency parameter [28] were also evaluated. However, as also found by Holdeman et al. [28] more traditional measures such as the pattern factor do not provide adequate sensitivity with respect to the mixing attempted.

The results obtained showed that changes in orifice size and spacing at a constant orifice-to-mainstream area ratio and momentum flux ratio have a significant influence on mixing effectiveness. Figure 5 displays the predicted nondimensionalized temperature

distributions on the center plane for three of the test cases with $Sc = 0.2$. The cases correspond to the minimum and maximum number of holes as well as the optimum configuration according to mixture uniformity. Also shown is a segment of the cross-sectional distribution at a downstream distance of one duct height, that is, $X/H = 1$ (the thin vertical black line on the center plane plot denotes an axial distance of one duct height downstream of the jets).

The first orifice configuration (Fig. 5a) shows that the opposing jets overpenetrate into the mainstream flow and impinge on each other, where after it is turned in the downstream direction. From the cross-sectional distribution at different planes it was observed that initially the mainstream air is forced to flow around the jets and toward the top and bottom walls and consequently does not mix with the jet flow effectively. As the flow continues downstream, the jets start to spread in the lateral direction and mixing occurs. However, at $X/H = 1$ it is evident from the θ values that the flow near the top and bottom walls is still unmixed. The ideal nondimensionalized equilibrium temperature was calculated using Eqs. (4) and (7) and equals 0.211. Contours corresponding to this value therefore indicate complete mixing.

Figure 5c constitutes the case where jet penetration becomes less as the number of orifices is increased, and the opposing jet flows only mix radially beyond an axial distance of one duct height. Flow from the closely spaced small orifices underpenetrates and remains near the top and bottom walls, opposite to the first orifice configuration. Although mixing is far from optimal, lateral mixing occurs much faster than radial mixing due to the closer spacing between orifices.

Optimum mixing was obtained when $S/H = 0.429$, corresponding to seven orifices as shown in Fig. 5b. The results show that the jets penetrate up to about a quarter of the duct height, and that mixing is rapid, both in the radial and lateral directions. At one duct height downstream from the orifices, complete mixing is almost achieved. Holdeman [16] defined $C = 1.25$ in Eq. (2) to achieve optimum mixing for opposed rows of in-line jets. It follows that the corresponding value of S/H at the chosen momentum flux ratio is 0.395 and implies that either seven or eight orifices will provide, theoretically, optimal mixing when $N = 7.6$. The numerical prediction is therefore in good agreement with the empirical relationship.

Figure 6 displays the results when $Sc = 0.85$ for the three test cases, that is, a minimum and maximum number of holes as well as the optimum configuration. The general trends observed as orifice size and spacing vary are the same. However, the degree of mixing

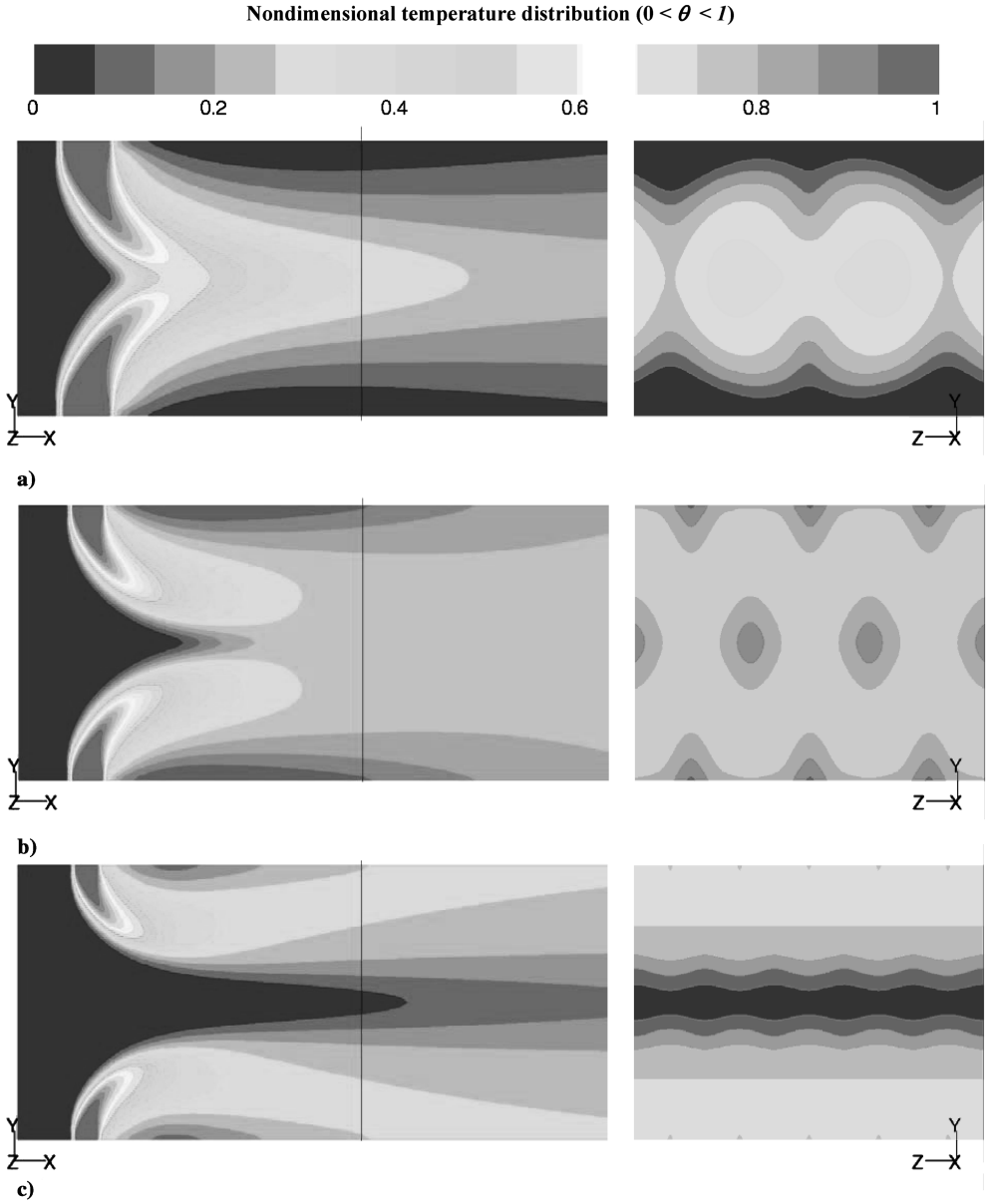

Fig. 5 Nondimensionalized temperature distributions on the center plane (left side) and cross-sectional plane (right side) one duct height downstream from the jet inlets with $Sc = 0.2$; a) $S/H = 1$; b) $S/H = 0.429$; c) $S/H = 0.25$. An axial distance of one duct height is denoted by the thin vertical black lines.

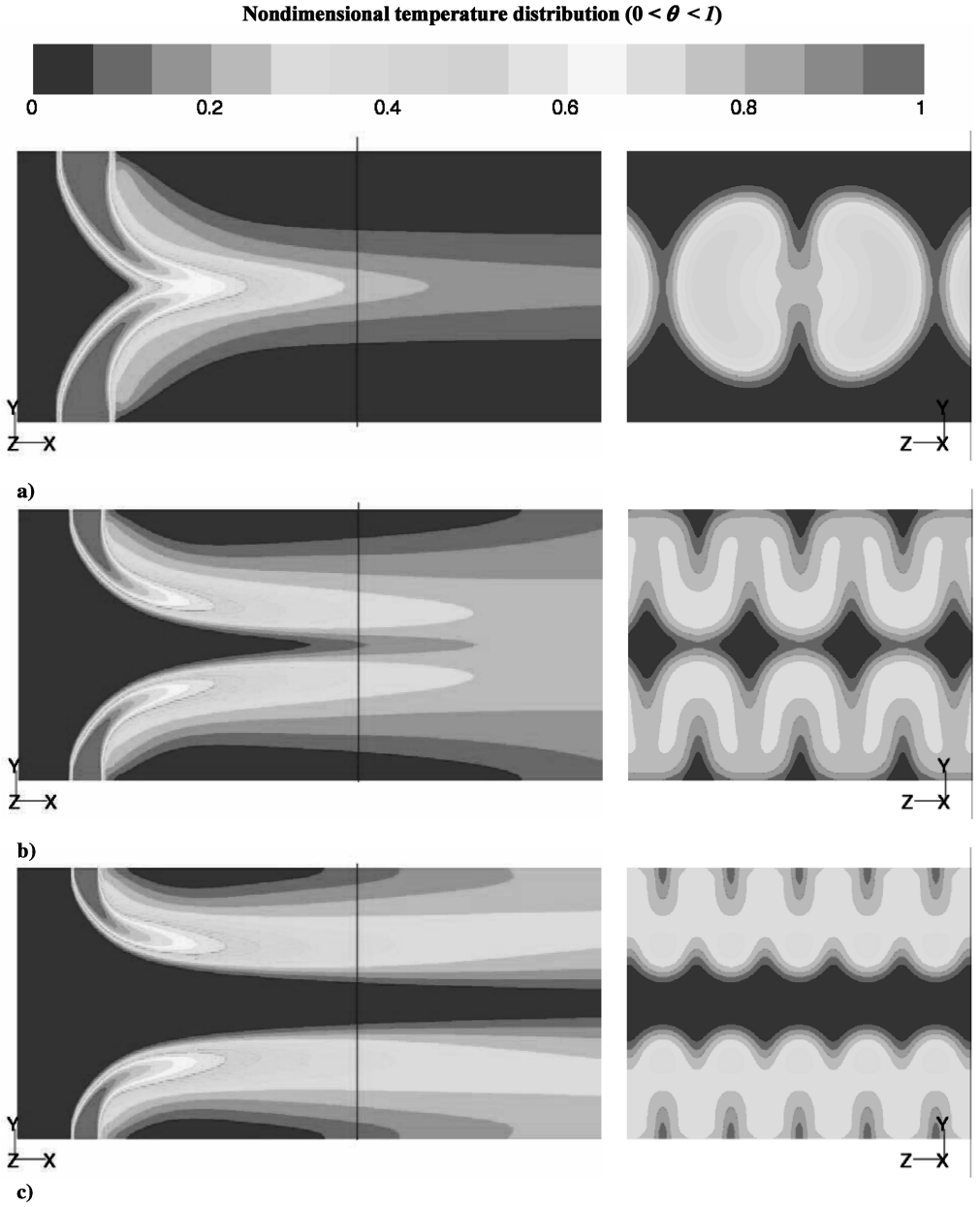

Fig. 6 Nondimensionalized temperature distributions on the center plane (left side) and cross-sectional plane (right side) one duct height downstream from the jet inlets with $Sc = 0.85$; a) $S/H = 1$; b) $S/H = 0.335$; c) $S/H = 0.25$. An axial distance of one duct height is denoted by the thin vertical black lines.

differs considerably and exhibits too little mixing compared to Fig. 5. Jet penetration is also more pronounced and penetrates farther into the crossflow. The optimum configuration was obtained when $S/H = 0.335$ which corresponds to nine orifices, although $S/H = 0.377$ (i.e., eight orifices) provided a similar degree of mixing efficiency.

A more quantitative description of mixture uniformity at the different planes along the length of the duct is shown in Fig. 7. The solid lines denote a turbulent Schmidt number of 0.2, whereas the dotted lines denote a turbulent Schmidt number of 0.85. The configuration of $S/H = 0.429$ is superior, except at $X/H = 0.25$. It should, however, be emphasized that the unmixedness curves of the other configurations not shown are more closely spaced along the optimal S/H curve. A more suitable definition of the overall mixture uniformity, also noted by Bain et al. [20], could be based on the integrated area under each unmixedness curve in Fig. 7. A single parameter can therefore be used to quantify the mixing effectiveness of a specific configuration. The importance of such a parameter becomes clearer when extended to mathematical optimization.

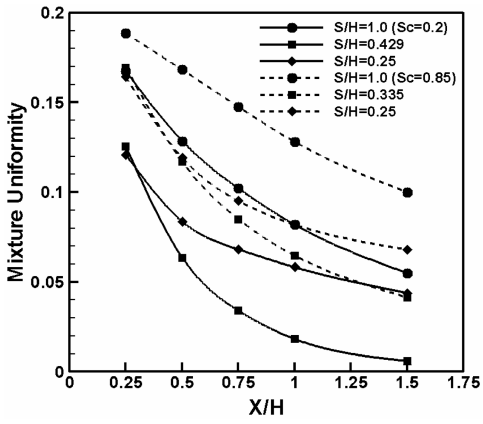

Fig. 7 Mixture uniformity at different cross-sectional planes.

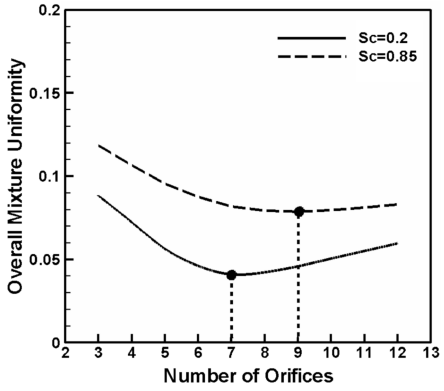

Fig. 8 Overall mixture uniformity.

Mathematical optimization requires the specification of a design criterion or objective function to be minimized with respect to chosen design variables, using an optimization algorithm. It can be concluded from Fig. 7 that two different results would be obtained if the design criterion was specified to be the mixture uniformity at $X/H = 0.25$ and if it were to be specified at $X/H = 1$. Similarly it is important to specify between which planes the integration is performed. Results obtained by integrating the cross-sectional planes at $X/H = 0.25$ and $X/H = 1$ are displayed in Fig. 8. The local minimum of seven orifices is clear and more pronounced when using a lower turbulent Schmidt number. Overall the results obtained compare favorably with the findings of previous investigations cited.

B. Mathematical Optimization

The typical design of a combustor involves numerous design parameters and variables, and multiple objectives such as obtaining low emission levels while establishing a temperature profile that is acceptable to the turbine. This needs to be done within a restrictive spatial domain and specified operating conditions, such as the overall pressure drop and maximum allowable liner temperature. Applying the above parametric approach would therefore rely heavily on the insight of the designer, and on a trial-and-error basis as the number of variables increases with an increase in multiple objectives and constraints.

However, such a multiparameter and multivariable problem lends itself naturally to the application of mathematical optimization techniques. These techniques allow, for a given set of parameters, the systematic adjustment of design variables to achieve improvement in performance, while automatically accounting for any constraints imposed on the system. In principle any appropriate computationally economic mathematical optimization algorithm may be used to perform the optimization. It should be economic, in terms of the number of iterations required for convergence, because of the computational cost associated with the simulations on which the optimization is to be based. Here the method of choice is the relatively new dynamic-Q algorithm, first introduced by Snyman et al. [32] and very recently refined by Snyman and Hay [33].

The algorithm was chosen for the following reasons. First of all, Snyman and Hay [33] thoroughly tested the method on a standard set of smooth test problems and compared its performance with that of the well-established sequential quadratic programming (SQP) method, and found its performance to be competitive, if not superior, to that of the SQP method. Secondly, this algorithm has already been extensively and successfully applied to computationally expensive simulation-based optimizations, where the objective function behavior is not necessarily smooth due to numerical noise, and where multiple local minima may also occur, as expected in the current case. Furthermore, the actual time that the optimization algorithm takes is negligible compared to that of the numerical simulations.

Some examples of the application of dynamic-Q to simulation-based optimization are the air pollution minimization CFD study of Craig et al. [34], the work on heat sink mass minimization of Visser and De Kock [35], as well as the very recent work of Els and Uys [36] on vehicle suspension system design, and that of Hay and Snyman [37] on the design of tendon-driven manipulators. The work of Visser and De Kock [35] is of particular interest here, because they successfully applied dynamic-Q to a problem where they simultaneously considered continuous and integer variables, that is, a mixed integer optimization problem. In their case the integer variable corresponded to the number of cooling fans, whereas in the current study the integer variable is the number of orifices.

Although the dynamic-Q method and its applications are, as indicated above, well documented in the literature, it is nevertheless necessary to assist the reader here by presenting a brief outline of the method and indicating how it is used for this study. The method involves the application of a dynamic trajectory algorithm for unconstrained minimization, adapted to handle constrained problems via an appropriate penalty function formulation. The method is applied to successive approximate quadratic subproblems of the original problem. The successive subproblems are constructed from sampling, at relatively high computational expense, the behavior of the constraint functions and/or objective function at successive approximate solution points in the design space. The subproblems, which are analytically simple, are solved quickly and reliably using the adapted dynamic trajectory method. Consider the typical and general inequality and equality constrained optimization problem of the following form:

$$\text{Minimize } f(\boldsymbol{x}), \qquad \boldsymbol{x} = [x_1, x_2, \ldots, x_n]^T, \qquad \boldsymbol{x} \in R^n \tag{8}$$

subject to the inequality constraints

$$g_j(\boldsymbol{x}) \le 0, \qquad j = 1, 2, \ldots, m \tag{9}$$

and equality constraints

$$h_k(\boldsymbol{x}) = 0, \qquad k = 1, 2, \ldots, r \tag{10}$$

The initial approximate or trial design is denoted by $\boldsymbol{x}^{(0)}$ and the solution to the problem by $\boldsymbol{x}^*$. The associated penalty function is defined by

$$p(\boldsymbol{x}) = f(\boldsymbol{x}) + \sum_{j=1}^{m} \alpha_j g_j^2(\boldsymbol{x}) + \sum_{k=1}^{r} \beta_k h_k^2(\boldsymbol{x})$$
$$\text{where } \alpha_j = \begin{cases} 0 & \text{if } g_j(x) \le 0 \\ \rho_j & \text{if } g_j(x) > 0 \end{cases} \tag{11}$$

and ρ_j and β_k are large positive numbers. For simplicity, the penalty parameters ρ_j and β_k take on the same positive value $\rho_j = \beta_k = \mu_i$. It can be shown that, as μ_i tends to infinity, the unconstrained minimum of $p(x)$ tends to the constrained minimum of the original problem defined by Eqs. (8–10). In the application of the dynamic trajectory method used here, and with the objective and gradient functions appropriately scaled, the penalty parameter μ_i is introduced at a certain specified value, here $\mu_i = 10^2$, and then increased to $\mu_i = 10^4$ when the intersection of active constraints is found. The dynamic trajectory method is applied to approximate subproblems as follows. Successive approximate quadratic subproblems, $P[l]$: $l = 0, 1, 2, \ldots$, are formed at successive design points $\boldsymbol{x}^{(l)}$, starting with an initial arbitrary design $\boldsymbol{x}^{(0)}$. Only the objective function approximation is explicitly discussed in what follows. Approximations $\hat{g}_j(\boldsymbol{x})$ for the inequality constraints $g_j(\boldsymbol{x})$ and the approximations $\hat{h}_k(\boldsymbol{x})$ to the equality constraint functions $h_k(\boldsymbol{x})$ may be obtained in a similar fashion. For the subproblem $P[l]$ the approximation $\hat{f}(\boldsymbol{x})$ to $f(\boldsymbol{x})$ may be given by

$$\hat{f}(\boldsymbol{x}) = f(\boldsymbol{x}^{(l)}) + \nabla^T f(\boldsymbol{x}^{(l)})(\boldsymbol{x} - \boldsymbol{x}^{(l)}) + \tfrac{1}{2}(\boldsymbol{x} - \boldsymbol{x}^{(l)})^T C_j^{(l)} (\boldsymbol{x} - \boldsymbol{x}^{(l)}) \quad \text{for } j = 1, 2, \ldots, m \tag{12}$$

where $\nabla f(\boldsymbol{x})$ denotes the gradient vector. The approximate Hessian matrix $(C_j^{(l)})$ is given by the diagonal matrix

$$C_j^{(l)} = \text{diag}\left(c_j^{(l)}, c_j^{(l)}, \ldots, c_j^{(l)}\right) = c_j^{(l)} I \tag{13}$$

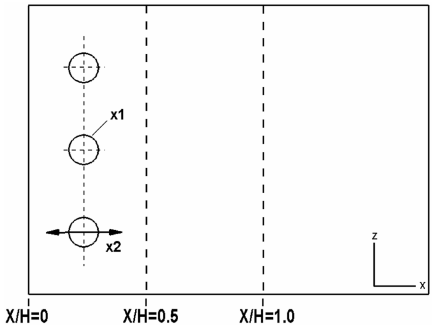

Fig. 9 Schematic representation of the design variables.

The initial values $c_j^{(0)}$ depend on the specific problem being considered. Here a value of 0.001 was arbitrarily used for the first subproblem. Thereafter the $c_j^{(l)}$ is calculated using the expression

$$c_j^{(l)} = \frac{2\{f(\boldsymbol{x}^{(l-1)} - f(\boldsymbol{x}^{(l)}) - \nabla^T f(\boldsymbol{x}^{(l)})(\boldsymbol{x}^{(l-1)} - \boldsymbol{x}^{(l)})\}}{\|\boldsymbol{x}^{(l-1)} - \boldsymbol{x}^{(l)}\|^2} \tag{14}$$

where $\|\cdot\|$ denotes the Euclidean norm. As a further aid in controlling convergence, intermediate move limits are imposed on the design variables during the minimization of the subproblem. These constraints are described by

$$x_i - x_i^{(l)} - \delta_i \le 0 - x_i + x_i^{(l)} - \delta_i \le 0, \qquad i = 1, 2, \ldots, n \tag{15}$$

The components of the gradient vector of the objective function at a specific design point $\boldsymbol{x}$, with respect to each of the design variables x_i, and used in the construction of the subproblem are approximated by the first-order forward differencing scheme

$$\frac{\partial f(\boldsymbol{x})}{\partial x_i} \approx \frac{f(\boldsymbol{x} + \Delta \boldsymbol{x}_i) - f(\boldsymbol{x})}{\Delta x_i}; \qquad i = 1, 2, \ldots, n \tag{16}$$

where $\Delta \boldsymbol{x}_i = [0, 0, \ldots, \Delta x_i, \ldots, 0]^T$ and Δx_i is a suitable step size usually determined from a sensitivity study. It is clear that $n + 1$ numerical analyses or function evaluations are required at each design point $\boldsymbol{x}$ to determine all the components of the objective gradient vector. The successive simple quadratic subproblems are solved economically using the latest version of the trajectory method [38] referred to above.

Consider the current problem of obtaining an optimum from the different test configurations in Table 2. Here, "optimum" is defined as the lowest mixture uniformity at a downstream distance of one duct height, that is, $X/H = 1$. Two design variables ($n = 2$) are considered, namely, the number of holes (x_1), as the spacing is implicitly defined as a result of the fixed total orifice area, and the axial position of the orifices (x_2) as shown in Fig. 9. Table 3 displays the upper and lower limits as well as the movement limits on these two design variables. In the current problem no explicit equality constraints were prescribed. It is, of course, obvious from Fig. 7 that the lowest mixture uniformity will most probably be obtained as x_2 approaches zero. The complete mathematical formulation of the relatively simple optimization problem to be considered in this preliminary feasibility study, is thus defined as

$$\begin{aligned} &\text{Minimize } [f(x) = \text{Mixture Uniformity } (\boldsymbol{x})] \\ &\text{subject to: } g_j = -x_j + x_j^{\min} \le 0, \qquad j = 1, 2 \\ &\qquad\qquad g_{j+2} = x_j - x_j^{\max} \le 0, \qquad j = 1, 2 \end{aligned} \tag{17}$$

Table 3 Upper and lower limits on the design variables and move limits

Design variable	Minimum	Maximum	Move limit
No. of holes (x_1)	3	12	1
X/H position (x_2)	0	0.5	0.1

where $x_j^{\min}$ and $x_j^{\max}$ denote the upper and lower limits on the variation of the variables.

Figures 10–12 display the results obtained by combining CFD simulations with mathematical optimization. Plotted in Fig. 10 are two typical convergence histories of the objective function, that is, mixture uniformity at $X/H = 1$, starting from two different initial approximate solutions to the problem. The optimization process shows, although the algorithm does not necessarily guarantee convergence to the global minimum, that in this simple case it appears to find it. In the first case $\boldsymbol{x}^{(0)} = [3, 0.39]^T$ and in the second case $\boldsymbol{x}^{(0)} = [11, 0.39]^T$. Although not imperative, the initial values were chosen here to lie below the upper limits, because first-order forward differencing is used in approximating the gradients used in constructing the subproblems.

Previous studies [39] have indeed demonstrated the robustness of the algorithm, being able to pull the design point into the feasible region, even if the initial point is infeasible. The results show that

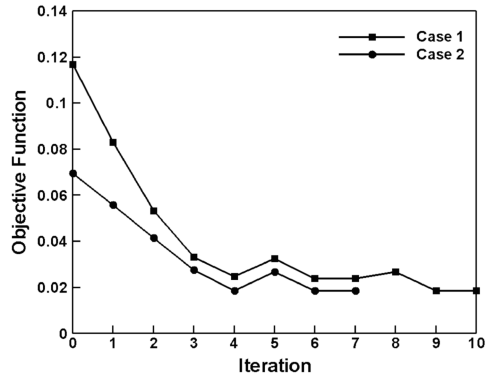

Fig. 10 Convergence history of the objective function starting from two different initial approximate solutions to the problem.

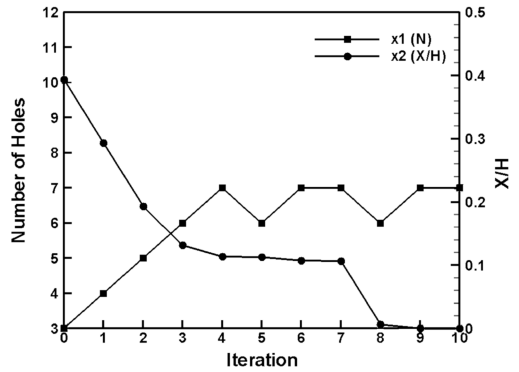

Fig. 11 Optimization history of the design variables initializing the algorithm with $\boldsymbol{x}^{(0)} = [3, 0.39]$.

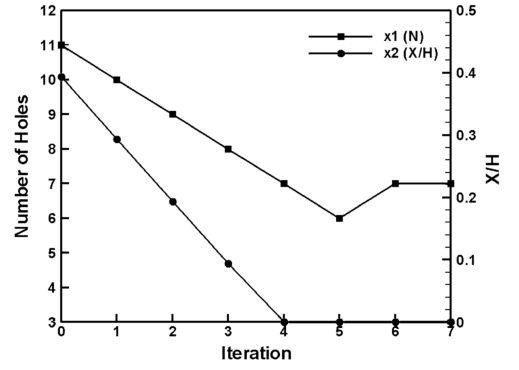

Fig. 12 Optimization history of the design variables initializing the algorithm with $\boldsymbol{x}^{(0)} = [11, 0.39]$.

for each case the optimization algorithm successfully and satisfactorily converges to an apparent global minimum. In the first case the optimum solution is essentially reached within 10 iterations (30 function evaluations), and in the second case within 7 iterations (21 function evaluations).

The number of iterations required for convergence is dependent upon the initial solution, as well as on the step size Δx_i. Although using a larger step size may result in fewer iterations, unreliable gradient information may be obtained, especially in the existing case where noise is present in the function. It is also possible to terminate the execution of the algorithm solution if the normalized step size or normalized change in function value is below a specified tolerance. Here, however, it was decided to allow the user to interactively terminate the optimization if, from observing the convergence history, no further significant improvement in the objection function occurs.

The corresponding convergence histories of the design variables for each case are shown in Figs. 11 and 12, respectively. In both cases a local optimum design of $x_1 = 7$ and $x_2 = 0$ is found that can be taken as the global optimum in this case. This is in agreement with the parametric results and empirical findings defined in Eq. (2). It should be noted that in observing the objective function convergence it is important to consider the history of the design variables in concurrence. The reason being that although the converged solution is taken to occur at a certain iteration, an equivalent feasible solution could be achieved at an earlier iteration step. Although not currently formulated, such introspective comparisons can be incorporated into the optimization algorithm to allow for automatic termination of the optimization process.

The robustness of the algorithm was also evaluated by initializing the solution with the optimum design variables. Considering the function evaluations, it was found that the solution oscillates around the optimum design point within the specified step size, indicating that an optimum design has been achieved. The oscillation is due to the algorithm taking integer steps in x_1, in attempting to improve the solution, but then repetitively returning to the previous better value of $x_1 = 7$.

IV. Conclusions

Numerical analyses of nonreacting opposed jets in crossflow have been performed using CFD and mathematical optimization. A validation study was conducted, comparing measured and predicted nondimensionalized temperature distributions to ensure that the CFD modeling techniques used are validated. The importance of specifying an appropriate turbulent Schmidt number, dependent on the jet-to-mainstream momentum flux ratio as well as downstream distance, was highlighted. At low jet-to-mainstream momentum flux ratios and turbulent Schmidt numbers of 0.85, peak values of the measured temperature distributions were overpredicted and consequently too little mixing exhibited. However, by lowering the turbulent Schmidt number to 0.2, good agreements were obtained between measurements and predictions for the same momentum flux ratio. At higher momentum flux ratios the influence of Sc is less pronounced and higher values more appropriate. This suggests that the turbulent Schmidt number should be treated as a variable within the solution.

The parametric CFD study evaluated the mixing effectiveness of various orifice configurations. The number of orifices and spacing in between the orifices varied, while keeping the momentum flux ratio and total orifice area constant. The results showed that changes in orifice size and spacing have a pronounced effect on mixing effectiveness. In between the two extreme cases of closely spaced small orifices and more widely spaced larger orifices lay an optimum configuration that provided the highest degree of mixing uniformity. It was found that the optimum configuration is in good agreement with empirically defined relationships.

Mathematical optimization techniques were then combined with CFD, as an alternative method to address the mixing effectiveness of different orifice configurations. The optimization method involved the application of a dynamic trajectory method for unconstrained optimization, adapted to handle constrained problems through appropriate penalty function formulations. The method converged successfully to a global optimum, which agreed with the results obtained from the parametric study. Although the numerical simulations are computationally expensive, the optimization algorithm has the distinct advantage of requiring relatively few function evaluations before reaching an optimal solution. Future work includes the introduction of more variables, multiple objectives, and design constraints such as the overall pressure drop.

References

[1] Kamotani, Y., and Greber, J., "Experiments on Confined Turbulent Jets in Cross Flow," NASA CR-2392, 1974.

[2] Holdeman, J. D., Srinivasan, R., and Berenfeld, A., "Experiments in Dilution Jet Mixing," *AIAA Journal*, Vol. 22, No. 10, 1984, pp. 1436–1443.

[3] Cluas, R. W., and Vanka, S. P., "Multigrid Calculations of a Jet in Crossflow," *Journal of Propulsion and Power*, Vol. 8, No. 2, 1992, pp. 425–431.

[4] Bain, D. B., Smith, C. E., Liscinsky, D. S., and Holdeman, J. D., "Flow Coupling Effects in Jet-in-Crossflow Flowfields," *Journal of Propulsion and Power*, Vol. 15, No. 1, 1999, pp. 10–16.

[5] Spencer, A., "Gas Turbine Combustor Port Flows," Ph.D. Dissertation, Aeronautical and Automotive Engineering and Transport Studies Department, Loughborough University, Loughborough, U.K., 1998.

[6] Srinivasan, R., Berenfeld, A., and Mongia, H. C., "Dilution Jet Mixing Program: Phase I Report," NASA CR-168031, 1982.

[7] Srinivasan, R., Coleman, E., and Johnson, K., "Dilution Jet Mixing Program: Phase II Report," NASA CR-174624, 1984.

[8] Srinivasan, R., Myers, G., Coleman, E., and White, C., "Dilution Jet Mixing Program: Phase III Report," NASA CR-174884, 1985.

[9] Srinivasan, R., and White, C., "Dilution Jet Mixing Program: Supplementary Report," NASA CR-175043, 1986.

[10] Holdeman, J. D., "Perspectives on the Mixing of a Row of Jets with a Confined Crossflow," AIAA Paper 83-1200, 1983; also NASA TM 83457.

[11] Holdeman, J. D., "Modeling Dilution Jet Flowfields," *Journal of Propulsion and Power*, Vol. 2, No. 1, 1986, pp. 4–10.

[12] Liscinsky, D. S., and True, B., "Experimental Investigation of Crossflow Jet Mixing in a Rectangular Duct," AIAA Paper 93-2037, 1993; also NASA TM 106152.

[13] Kroll, J. T., Sowa, W. A., Samuelsen, G. S., and Holdeman, J. D., "Optimization of Circular Orifice Jets Mixing into a Heated Cross Flow in a Cylindrical Duct," AIAA Paper 93-0249, 1993; also NASA TM 105984.

[14] Hatch, M. S., Sowa, W. A., Samuelsen, G. S., and Holdeman, J. D., "Jet Mixing into a Heated Cross Flow in a Cylindrical Duct: Influence of Geometry and Flow Variations," AIAA Paper 92-0773, 6–9 January 1992; also NASA TM 105390.

[15] Holdeman, J. D., Reynolds, R., and White, C., "A Numerical Study of the Effects of Curvature and Convergence on Dilution Jet Mixing," AIAA Paper 87-1953, 1987; also NASA TM 89878.

[16] Holdeman, J. D., "Mixing of Multiple Jets with a Confined Subsonic Crossflow," *Progress in Energy and Combustion Science*, Vol. 19, 1993, pp. 31–70.

[17] Liscinsky, D. S., and True, B., "Enhanced Mixing in a Rectangular Duct," NASA CR-212320, 2003.

[18] Oechsle, V. L., "Mixing and NOx Emission Calculations of Confined Reacting Jet Flows in a Cylindrical Duct," NASA CR-212321, 2003.

[19] St. John, S., and Samuelsen, G. S., "Detailed Studies of the Quick Mixing Region in Rich Burn Low-NOx Combustion," NASA CR-212316, 2003.

[20] Bain, D. B., Smith, C. E., and Holdeman, J. D., "CFD Mixing Analysis of Axially Opposed Rows of Jets Injected into Confined Crossflow," AIAA Paper 93-2044, 1993; also NASA TM 106179.

[21] Bain, D. B., Smith, C. E., and Holdeman, J. D., "CFD Mixing Analysis of Jets Injected from Straight and Slanted Slots into Confined Crossflow in Rectangular Ducts," AIAA Paper 92-3087, 1992; also NASA TM 105699.

[22] Bain, D. B., Smith, C. E., and Holdeman, J. D., "CFD Assessment of Orifice Aspect Ratio and Mass Flow Ratio on Jet Mixing in Rectangular Ducts," AIAA Paper 94-0218, 1994; also NASA TM 106434.

[23] Bain, D. B., Smith, C. E., and Holdeman, J. D., "Jet Mixing and Emission Characteristics of Transverse Jets in Annular and Cylindrical Confined Crossflow," AIAA Paper 95-2995, 1995; also NASA TM 106976.

[24] Holdeman, J. D., Liscinsky, D. S., Oechsle, V. L., Samuelsen, G. S., and Smith, C. E., "Mixing of Multiple Jets with a Confined Subsonic Crossflow in a Cylindrical Duct," ASME Paper 96-GT-482, 1996; also NASA TM 107185.
[25] De Kock, D. J., Craig, K. J., and Pretorius, C. A., "Mathematical Maximisation of Minimum Residence Time for Two Strand Continuous Caster," *Ironmaking and Steelmaking*, Vol. 30, No. 3, 2003, pp. 229–234.
[26] De Kock, D. J., and Visser, J. A., "Trade-Off Design of Extruded Heat Sinks Using Mathematical Optimization," *Journal of Electronic Packaging*, Vol. 126, Sept. 2004, pp. 333–341.
[27] FLUENT, Software Package, Ver. 6.2.16, Fluent Inc., Lebanon, NH, 2004.
[28] Holdeman, J. D., Walker, R. E., and Kors, D. L., "Mixing of Multiple Dilution Jets with a Hot Primary Airstream for Gas Turbine Combustors," AIAA Paper 73-1249, 1973.
[29] He, G., Guo, Y., and Hsu, A. T., "The Effect of Schmidt Number on Turbulent Scalar Mixing in a Jet-in-Crossflow," *International Journal of Heat and Mass Transfer*, Vol. 42, No. 20, 1999, pp. 3727–3738.
[30] Anand, M. S., Zhu, J., Connor, C., and Razdan, M. K., "Combustor Flow Analysis Using an Advanced Finite-Volume Design System," ASME Paper 99-GT-273, 1999.
[31] Lefebvre, A. H., *Gas Turbine Combustion*, Hemisphere Publishing Corp., Washington, D.C., 1983, p. 142.
[32] Snyman, J. A., Stander, N., and Roux, W. J., "A Dynamic Penalty Function Method for the Solution of Structural Optimisation Problems," *Applied Mathematical Modelling*, Vol. 18, No. 8, 1994, pp. 453–460.
[33] Snyman, J. A., and Hay, A. M., "The Dynamic-Q Optimization Method: An Alternative to SQP?," *Computers and Mathematics with Applications*, Vol. 44, No. 12, 2002, pp. 1589–1598.
[34] Craig, K. J., De Kock, D. J., and Snyman, J. A., "Using CFD and Mathematical Optimization to Investigate Air Pollution due to Stacks," *International Journal for Numerical Methods in Engineering*, Vol. 44, No. 4, 1999, pp. 551–565.
[35] Visser, J. A., and De Kock, D. J., "Optimization of Heat Sink Mass Using the Dynamic-Q Numerical Optimization Method," *Communications in Numerical Methods in Engineering*, Vol. 18, No. 10, 2002, pp. 721–727.
[36] Els, P. S., and Uys, P. E., "Investigation of the Applicability of the Dynamic-Q Optimization Algorithm to Vehicle Suspension Design," *Mathematical and Computer Modelling*, Vol. 37, Nos. 9–10, 2003, pp. 1029–1046.
[37] Hay, A. M., and Snyman, J. A., "Optimization of a Planar Tendon-Driven Manipulator for a Maximal Dextrous Workspace," *Engineering Optimization*, Vol. 37, No. 3, 2005, pp. 217–236.
[38] Snyman, J. A., "The LFOPC Leap-Frog Algorithm for Constrained Optimisation," *Computers and Mathematics with Applications*, Vol. 40, No. 8, 2000, pp. 1085–1096.
[39] Craig, K. J., De Kock, D. J., and Gauche, P., "Minimization of Heat Sink Mass Using Mathematical Optimization," *ASME Journal of Electronic Packaging*, Vol. 121, No. 3, 1999, pp. 143–147.

J. Oefelein
Associate Editor